Hindawi
Advances in Civil Engineering
Volume 2019, Article ID 7467920, 19 pages
https://doi.org/10.1155/2019/7467920

Research Article

Fragility Analysis of a Self-Anchored Suspension Bridge Based on Structural Health Monitoring Data

Yuyao Cheng,[1] **Jian Zhang**,[1,2] **and Jiajia Wu**[1]

[1]*School of Civil Engineering, Southeast University, Nanjing 210096, China*
[2]*Jiangsu Key Laboratory of Engineering Mechanics, Southeast University, Nanjing 210096, China*

Correspondence should be addressed to Jian Zhang; jian@seu.edu.cn

Received 7 May 2019; Revised 26 July 2019; Accepted 20 August 2019; Published 29 September 2019

Academic Editor: Andreas Lampropoulos

This paper presents an improved fragility analysis methodology to estimate structural vulnerability for probabilistic seismic risk assessment. Three main features distinguish this study from previous efforts. Firstly, the updated fragility curves generated are based on experimental measurements and possess higher accuracy than those produced using design information only. The updated fragility curves take into consideration both the geometry and material properties, as well as long-term health monitoring data, to reflect the current state of the structure appropriately. Secondly, to avoid arbitrariness when selecting ground motions, probabilistic seismic hazard analysis (PSHA) is adopted to provide suggestions for ground motion selection. By considering the uncertainty of the location and intensity of future earthquakes, the PSHA deaggregation result can help to determine the most probable earthquake scenarios for the specific site. Thus, the suggested ground motions are more realistic, and the seismic demand model is much closer to the actual results. Thirdly, this study focuses on the seismic performance evaluation of a typical self-anchored suspension bridge using the form of fragility curves, which has seldom been studied in the literature. The results show that bearing is the most vulnerable part of a self-anchored suspension bridge, while failure probabilities of concrete towers are relatively lower.

1. Introduction

Fragility curves are an important tool for representing the vulnerability of bridge structures in probabilistic seismic risk assessment. The curves are defined as a function of ground motion intensity parameters, such as peak ground acceleration (PGA) and spectral acceleration (SA), to describe the probability of exceeding a damage state. Three main methods have been developed to build fragility functions: expert opinion, empirical judgment, and analytical techniques [1–6]. For bridges located in regions where past earthquake damage information is absent, the analytical technique is the only proper method to calculate the fragility curve [7]. A significant number of studies have investigated the development of fragility curves using analytical techniques [8–10]. Pan et al. [11] investigated the seismic fragility of typical multispan continuous and simply supported bridges in the state of New York for damage states corresponding to failure of piers and steel bearings. Parool and Rai [12] used the archetype model of a multispan simply supported bridge with drop spans and steel bearings to demonstrate the seismic vulnerability can be significantly reduced in such bridges if the steel bearings are replaced with elastomeric pads. Mosleh et al. [13] generated fragility curves for one of the most common bridge typologies, to investigate the seismic performance of RC bridges built before the 1990s. In addition, some studies have focused on the seismic fragility of cable-stayed bridges using the analytical method. Li et al. [14] evaluated the seismic performance of a sea-crossing cable-stayed bridge using the fragility function methodology. Pang et al. [15] studied the seismic fragility of cable-stayed bridges considering different sources of uncertainties based on the uniform design method. Choine et al. [16] made a seismic reliability assessment of reinforced

concrete integral bridges subject to corrosion, and Ghosh and Sood [17] studied the degradation models for seismic fragility assessment of aging highway bridges.

Despite previous efforts to generate fragility curves using analytical models, fragility curves based only on design information may not represent the current behavior of the in-service structure. In addition, these curves fail to consider phenomena derived from structural stiffness degradation due to aging factors. With the advent of structural health monitoring (SHM) techniques, the dynamic properties of the bridge in its current state can be identified and monitored, providing the opportunity to generate a model with greater accuracy. Torbol et al. [18] built fragility curves for highway bridges based not only on geometry and material properties but also on vibration data recorded by a structural health monitoring system. However, this research focused only on regular girder bridges. Karapetrou et al. [19] used monitoring data in model updating for the fragility analysis of a hospital RC building. As an important part of the existing transportation network, the seismic performance evaluation of suspension bridges using the form of fragility curves is less studied. Only Sgambi et al. [20] have recently carried out the seismic analysis of a long-span cable-suspended bridge considering the variability of certain factors related to the seismic input. Karmakar et al. [21] investigated the probabilistic seismic behavior of the Vincent Thomas suspension bridge after a major retrofit.

It is inappropriate to apply existing conclusions derived from regular girder bridges to suspension bridges directly, especially for different types of suspension bridges. Thus, more specialized research must focus on the suspension bridge type to assess seismic fragility and suggest possible retrofitting solutions if required.

In addition, insufficient attention has been paid to the selection of ground motions, which is one of the most important factors for generation of the fragility curves. Synthetic motion is mostly used as ground motion in seismic demand analysis [22, 23], or it is randomly selected from the PEER database of existing research [18, 24, 25]; in this case, the chosen input may not be the most likely earthquake at the site. By considering all areas where earthquakes may occur, and the possibility of earthquakes occurring with various magnitudes, probabilistic seismic hazard analysis (PSHA) has been identified as an effective method to best estimate site-specific hazards, and the follow-up hazard deaggregation results can provide the most probable scenario for the site [26]. Through this process, proper earthquake motions can be appropriately selected.

This study has two primary objectives. The first is to generate fragility curves for the self-anchored suspension bridge using properly selected ground motions based on the results of seismic hazard deaggregation analysis. The second objective is to demonstrate the practical use of structural health monitoring data in seismic vulnerability analysis, achieving an updated fragility curve. This article is organized as follows: The proposed fragility methodology combined with PSHA and SHM data is first introduced. Secondly, a typical self-anchored suspension bridge is chosen to be investigated by using the proposed method, and its SHM system is illustrated briefly. The initial finite element (FE) model is then established based on the design information and is updated according to the experimental data recorded from both static and dynamic testing to achieve a more accurate model which can reflect the current state. Finally, fragility curves for the updated model are calculated.

2. Proposed Procedure of Fragility Analysis

To obtain analytical fragility curves, three steps should be considered: the simulation of ground motions, the simulation of bridges, and the generation of fragility curves. As illustrated in Figure 1, in the proposed method, PSHA is conducted to estimate the probability of different intensity earthquakes occurring at the specific site, and follow-up hazard deaggregation analysis is performed to determine the most probable seismic scenario, providing the basis for ground motion selection. Monitoring data recorded from both the static test and the dynamic measurement are then utilized to update the initial model to achieve a more accurate one, which can reflect the current state of the in-service structure. The framework of the proposed method combined with PSHA and SHM data is illustrated in detail in Figure 1.

Adequate selection of ground motions is vital to obtain a more accurate prediction of a structure's seismic response. Selection based on deaggregation analysis, which is an in-depth PSHA study for the site, is suggested here as it can determine the most likely future seismic scenario. In this situation, the selected ground motions are more realistic, and the seismic demand model is closer to the actual ones. The representative method of PSHA was proposed by Cornell [27] and McGuire and Arabasz [28] and takes the uncertainties of earthquake magnitude (M), source-to-site distance (D), and wave attenuation into account. The expression is as follows:

$$P(Y > y) = \sum_{i=1}^{N_s} v_i \sum_{j=1}^{N_M} \sum_{k=1}^{N_D} P_r\left[Y > y \mid m_j, d_k\right] \times P_r\left[M = m_j\right] \times P_r\left[D = d_k\right], \tag{1}$$

where N_S, N_M, $and\, N_D$ are the number of sources, magnitude bins, and distance bins, respectively; v is the annual earthquake rate governed by $v = 10^{a-bm}$, in which a value and b value are known as the G-R recurrence parameters; $P_r[Y > y \mid m_j, d_k]$ represents the probability of the ground motion intensity Y exceeding specific intensity y with magnitude m_j and source-to-site distance d_k; and $P_r[M = m_j]$ and $P_r[D = d_k]$ are the probability of the specific earthquake magnitude and distance, respectively. Deaggregation is used in PSHA for analyzing hazard contributions from certain sizes and locations. The United States Nuclear Regulatory Commission [29] has recommend a deaggregation table by dividing magnitude into six magnitude range bins: 0~5, 5~5.5, 5.5~6, 6~6.5, 6.5~7, and >7. Distance is also divided into distance range bins: 0~15, 15~25, 25~50, 50~100, 100~200, and >200.

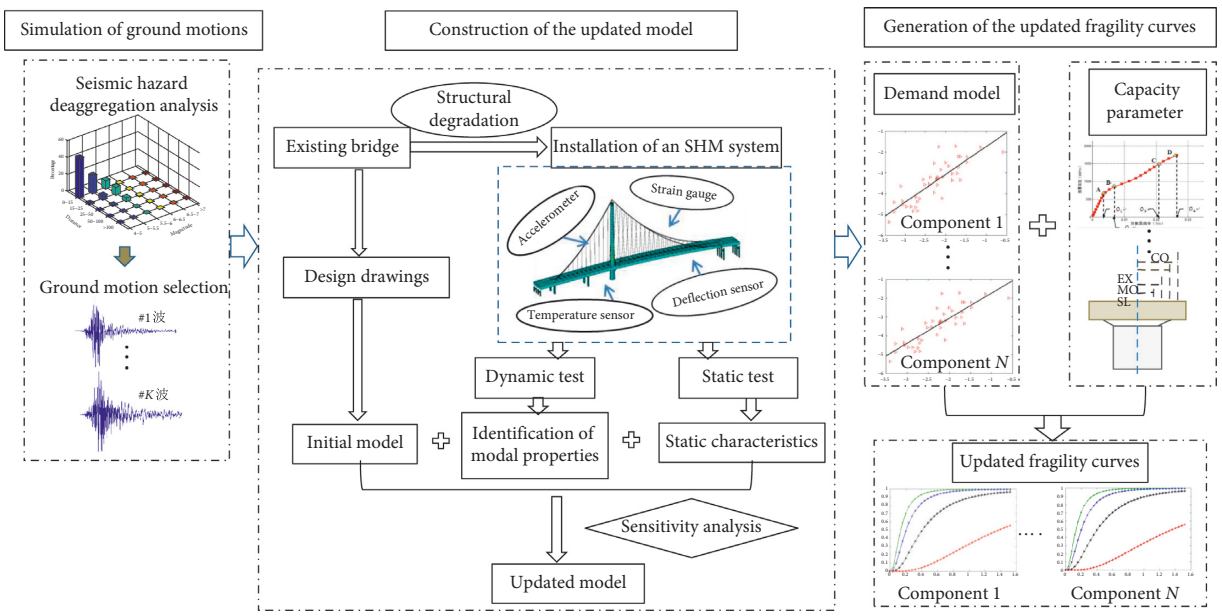

Figure 1: Framework of the proposed method.

Once the ground motions are selected, an accurate FE model must be constructed. Experiment measurements can be used to update the initial model to better reflect the current conditions of the structure. Dynamic testing can reflect the overall information on the structures; however, its inherent limitations hinder its development. Static tests have the advantage of high accuracy and low noise interference, but testing must be carried out within the elastic range. Therefore, an FE model updating method taking both static and dynamic tests into consideration is suggested in this study and can overcome the deficiencies of using static or dynamic test data separately.

According to the updated model, fragility curves are generated to represent the vulnerability of a bridge with a higher accuracy. Currently, the scaling approach and the cloud approach are the two most frequently used mechanisms to develop fragility curves based on nonlinear dynamic analysis [30]. The latter is adopted in this study as the scaling approach is too complicated for practical application. In the cloud approach, both the seismic demand and capacity of the structure are considered as random variables and assumed to be lognormal distributions. The structural capacity parameter can be estimated using available studies or probabilistic $M-\phi$ analysis. For the seismic demand model, the engineering-demand parameters (EDPs) can be combined with corresponding intensity measures (IMs), to build the power probabilistic seismic demand model (PSDM) [31]:

$$\begin{aligned} \overline{\mathrm{EDP}} &= a\mathrm{IM}^b \\ \text{or } \ln(\overline{\mathrm{EDP}}) &= \ln(a) + b\cdot\ln(\mathrm{IM}), \end{aligned} \tag{2}$$

where a value and b value are estimated parameters from linear regression analysis and $\overline{\mathrm{EDP}}$ is the median estimate of the seismic demand. To account for the uncertainty of the PSDM, the dispersion of the seismic demand $\beta_{\mathrm{EDP|IM}}$ is calculated by the following equation [25]:

$$\beta_{\mathrm{EDP|IM}} = \sqrt{\frac{\sum\left[\ln(D_i) - \ln(\overline{\mathrm{EDP}})\right]^2}{N-2}}, \tag{3}$$

where N is the number of nonlinear time-history analyses and D_i is the ith realization of structural demand.

The conditional probability of the bridge demand exceeding the capacity for a given intensity can be calculated using the followed formula:

$$P_f = \Phi\left[\frac{\ln(\overline{\mathrm{EDP}}) - \ln(S_{\mathrm{C}})}{\sqrt{\beta^2_{\mathrm{EDP|IM}} + \beta^2_{\mathrm{C}}}}\right], \tag{4}$$

where $\Phi[\cdot]$ is the standard normal cumulative distribution function, S_{C} is the median value of the seismic capacity, and β_{C} is the logarithmic standard deviation of the capacity.

The main motivating factor for this study is to demonstrate the practical application of SHM data and in-depth PSHA technique to evaluate the fragility of the self-anchored suspension bridge and to generate accurate fragility curves according to actual experiment data instead of only design information. A typical self-anchored suspension bridge located in Nanjing, China, is selected as a case study to verify the suitability of the proposed fragility analysis method.

3. The Studied Suspension Bridge and Its SHM System

3.1. Bridge Description. The investigated bridge (Figure 2) is a self-anchored suspension bridge with a length of 35 + 77 + 60 + 248 + 35 m. It consists of one single concrete tower, two main girders, and five additional concrete piers. The two main girders are connected with multiple crossbeams to form a stringer and horizontal system. In the main span, the girders are steel box girders, while prestressed concrete box girders are used in the side span and anchor span. The main cable includes two parts in the transverse

Figure 2: The investigated suspension bridge. (a) Side view. (b) Bottom of the girder. (c) E-type elastic-plastic damping bearings.

direction of the bridge and is anchored in the middle of the cross-beam in the side span. For the main span, the spatial cables are anchored to the ends of the beam. It is worth noting that a new kind of elastic-plastic energy-dissipating bearing was applied to the seismic isolation design of this bridge (Figure 2(c)). This new type of bearing integrates the E-type or C-type soft steel damper with the bearing so that it has the function of vertical support and horizontal hysteretic energy dissipation. In the transverse direction, bearings #7~9 and #11~12 are equipped with E-type elastic-plastic damping bearings to absorb lateral vibration. For bearing #10, two laminated rubber bearings are used to limit the lateral displacement of the bridge. In the longitudinal direction, the floating type is chosen, and only two elastic-plastic dampers are anchored on the #10 bearing for vibration absorption.

3.2. The SHM System. An SHM system was installed on the investigated bridge which included 80 sensors, and the layout plan is presented in Figure 3. A total of twenty uniaxial accelerometers (ACs) are used: Twelve are mounted on the internal box girder at 1/4, 1/2, and 3/4 sections of the main-span girder. Both north and south spans are monitored, and four are installed on the slings DS11 and DS15 in both horizontal and vertical directions. One AC is mounted on the cable near the main tower, and three are set on the top of the tower. Ten displacement sensors (DISs) are installed at 1/4, 1/2, and 3/4 sections of the main span, and 1/3 section of the side span, to measure the deformation of the bridge. In addition, seven sections including 1/8, 2/8, 3/8, 4/8, 5/8, 6/8, and 7/8 of the main span are selected to lay the prism to measure the displacement of the bridge in static testing. Twenty-seven strain gauges are placed at 1/2, 3/4, and 7/8 sections of the middle main span, and 16 strain gauges are mounted on 1/3 section of the two left side spans.

Based on the monitoring system, both the static property and dynamic characteristics of the investigated bridge are studied. The static test is conducted by loading a fleet of trucks with a weight of 30 t onto the bridge. The truck model is shown in Figure 4(c). The trucks are placed along the longitudinal direction, and according to the location of trucks, two different loading cases are considered. The first case is loading at 101.4 m from the tower, and the second is loading at 135 m from the tower. In the transverse direction, symmetrical loading and lateral eccentric loading in the south span are separately conducted in each case (Figure 4). The deflection of seven sections (1/8, 2/8, 3/8, 4/8, 5/8, 6/8, and 7/8 of the main span) is measured, and four measurement points are arranged in each section, as illustrated in Figure 4(d). The test results are provided in the subsequent section for comparison with the simulated results.

In the dynamic test, the ambient vibration data recorded by the accelerator mounted on the north of the 1/4 section of the main span are illustrated in Figure 5(a). The Complex Mode Indicator Function (CMIF) method is selected to identify the basic modal parameters. The first three frequencies are identified as 0.4348 Hz, 0.6799 Hz, and 1.2927 Hz.

The acceleration time history and power spectrum of the cable DS15 are plotted in Figures 5(c) and 5(d), respectively. The natural vibration frequency can be identified by picking the peaks of the power spectrum, and the cable force with fixed ends can then be obtained by the following formula:

$$T = 4\frac{m f_n^2 l^2}{n^2} - \frac{n^2\pi^2 \mathrm{EI}}{l^2}, \tag{5}$$

where EI is the bending stiffness of the cable, l is the cable length, and f_n is the nth natural frequency. Similarly, for the sake of simplicity, the value of the measured cable force will be provided in the subsequent section.

3.3. Finite Element Modeling. Prior to model updating, it is recommended that an initial model is obtained using the first available set of design information. The initial model of

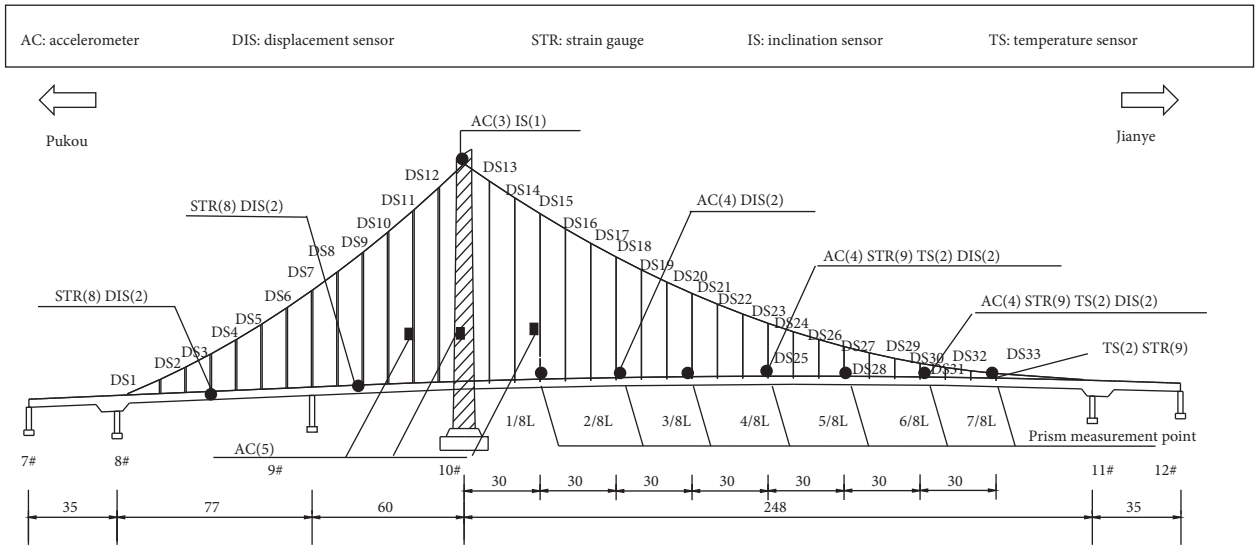

Figure 3: SHM system of the bridge.

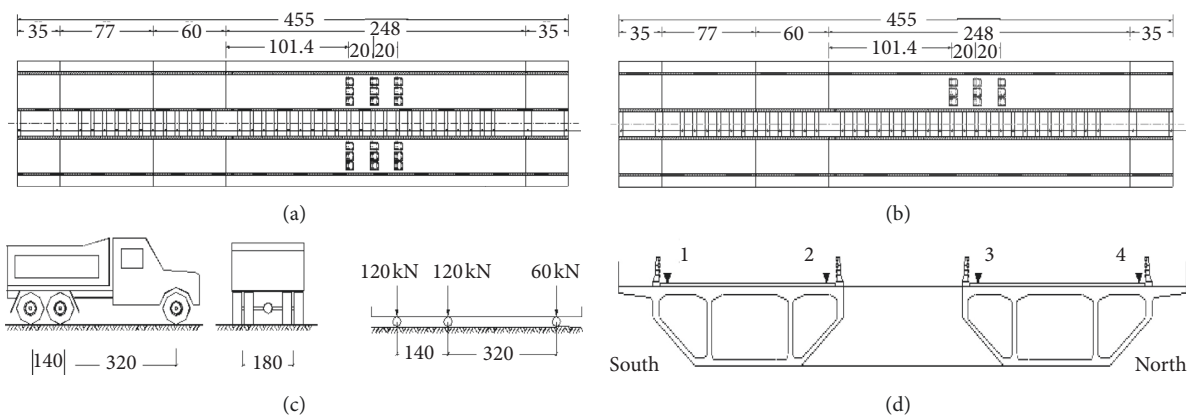

Figure 4: Cases of the static test. (a) Symmetric loading. (b) Partial loading. (c) Truck model. (d) Layout plan of measurement.

the suspension bridge is built using the ANSYS software. A detailed configuration of the bridge and modeling of some important components are shown in Figure 6. It is assumed in this study that the main girders maintain elasticity under the earthquake, but nonlinearities of the concrete towers and elastic-plastic damping bearings are considered. As the piers are set on the shore and the height is short because of the influence of the longitudinal slope and riverbed topography, the pier stiffness is too large to form a plastic hinge. Accordingly, for the sake of simplicity and reduction of computational time, the piers are also assumed to be linear in this study.

Elastic-plastic energy-dissipating bearings are installed on the bridge in both lateral and longitudinal directions. The layout plan of the bearing system is presented in Figure 6(e). In nonlinear analysis, the hysteretic curves are simplified as a bilinear model, and the force-deformation skeleton curve is illustrated in Figure 6(f), where it can be seen that the curve depends only on the yield load F_y. In this study, the combined 39 elements are chosen to simulate the nonlinearities of the new bearing type. Details of the bearing parameter are illustrated in Table 1.

The Solid 65 element is widely used to simulate nonlinearities of reinforced concrete components. As the element number of the solid model is too high and leads to convergence difficulty, a simplified tower model is adopted to improve computational efficiency. A detailed tower model (Figure 7(a)) is established by using the Solid 65 element, while a simplified model (Figure 7(b)) is constructed using the Beam 188 element. For the detailed model, the reinforcement of the section is shown in Figure 7(a) (2) and includes three layers of reinforcement: the outer, middle, and inner. The constitutive relationship of the steel and concrete is shown in Figure 7(a) (3-4). Pushover analysis is then carried out on these two models, and the displacement of the tower top is made to approach each other by adjusting the material parameters of the simplified model. The appropriate stress-strain relationship is determined once the displacement of the tower top is overlapped (Figure 7(c)). Thus, it can be concluded that this simplified model

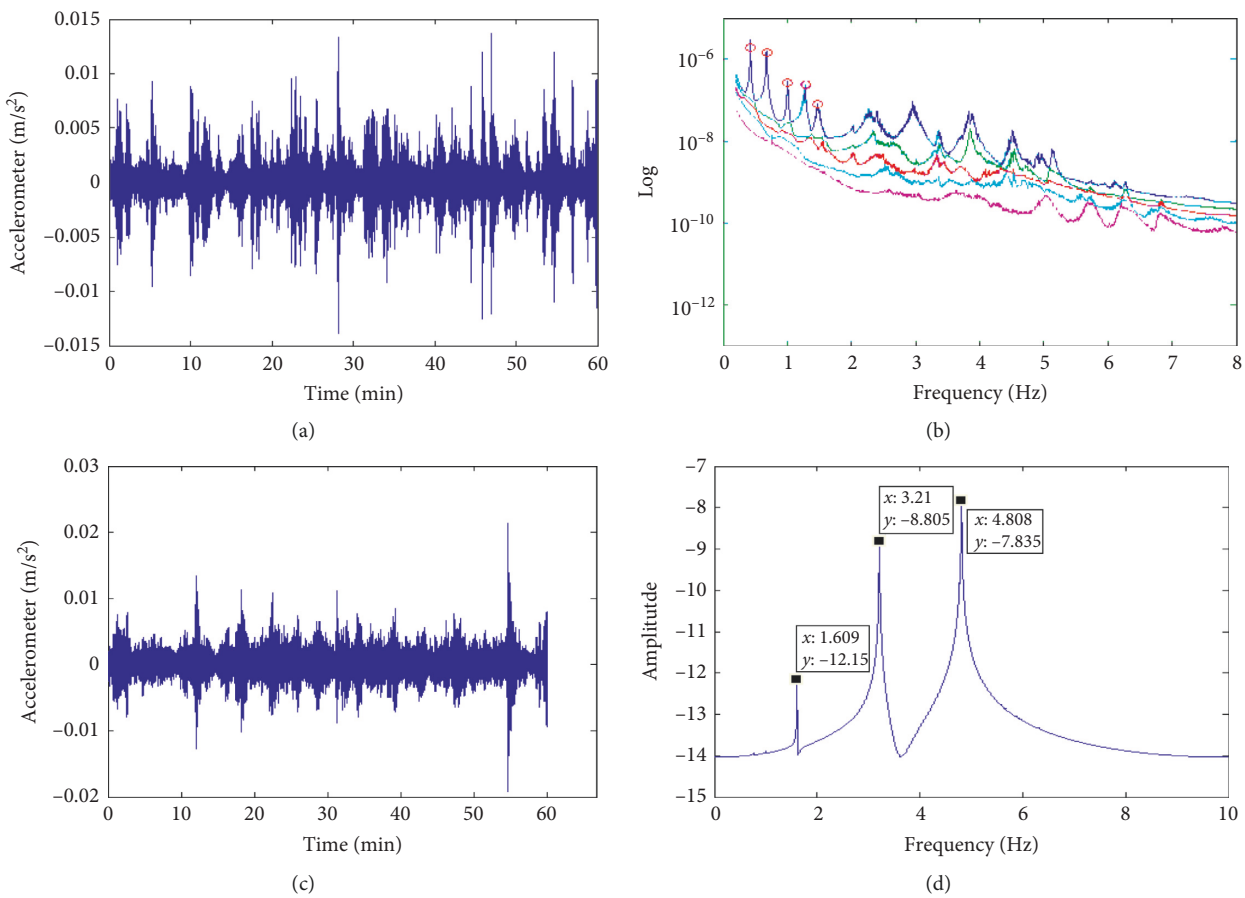

Figure 5: Ambient vibration test. (a) Acceleration time history at 1/4 section of the main girder. (b) CMIF. (c) Acceleration time history of the sling. (d) Acceleration power spectrum of the sling.

coincides with the detailed model. Finally, the simplified tower model substitutes the detailed model to form the full bridge model combined with other components. To account for the sag effect of the cable system, the cable element is modeled as LINK10 with modified elasticity modulus. Rigid links are used to connect the cables to the tower.

3.4. Sensitivity Analysis of the Parameters. The selection of updating parameters is a key step in FE model updating. The uncertainties of material parameters, boundary conditions, and geometric parameters are critical and must be considered. To avoid huge calculation amounts in the optimization process due to blind selection, sensitivity analysis is executed to find the parameters that will cause a large change in the structural characteristics when varying their assigned value in the FE model. The state function is defined as $f_r = f(x_1, x_2, \ldots, x_n)$, and then the sensitivity of different parameters can be obtained by taking the partial derivative of the function:

$$\nabla f_r = \left\{\frac{\partial f_r}{\partial x_1}, \frac{\partial f_r}{\partial x_2}, \ldots, \frac{\partial f_r}{\partial x_n}\right\}, \tag{6}$$

where

$$\frac{\partial f_r}{\partial x_i} = \frac{f(x + \Delta x_i e) - f(x)}{\Delta x_i}. \tag{7}$$

In this study, the cross-sectional area and the mass of the bridge are assumed to remain unchanged unless changes are visually discernible. The elastic modulus of the main girder, tower, pier, main cable, and sling (E_g, E_t, E_p, E_c, and E_s), as well as the initial strain of the sling, cable, and girder (I_s, I_c, and I_g), and the stiffness of the transversal damper and longitudinal damper (K_t and K_l) are selected. Figure 8 illustrates the sensitivity of the static property (static deformation) and dynamic characteristics (frequency and cable force) to changes in the updated parameters.

The sensitivity analysis reveals that the elastic modulus of the cable is highly sensitive to static deformation, and the variation of the main girder's elastic modulus causes the largest change in the natural frequency. The parameters of the tower, sling, and pier can be disregarded as they are insensitive to the structural response in both the static and dynamic tests. The stiffness of the damper affects response with different degrees and so should also be considered.

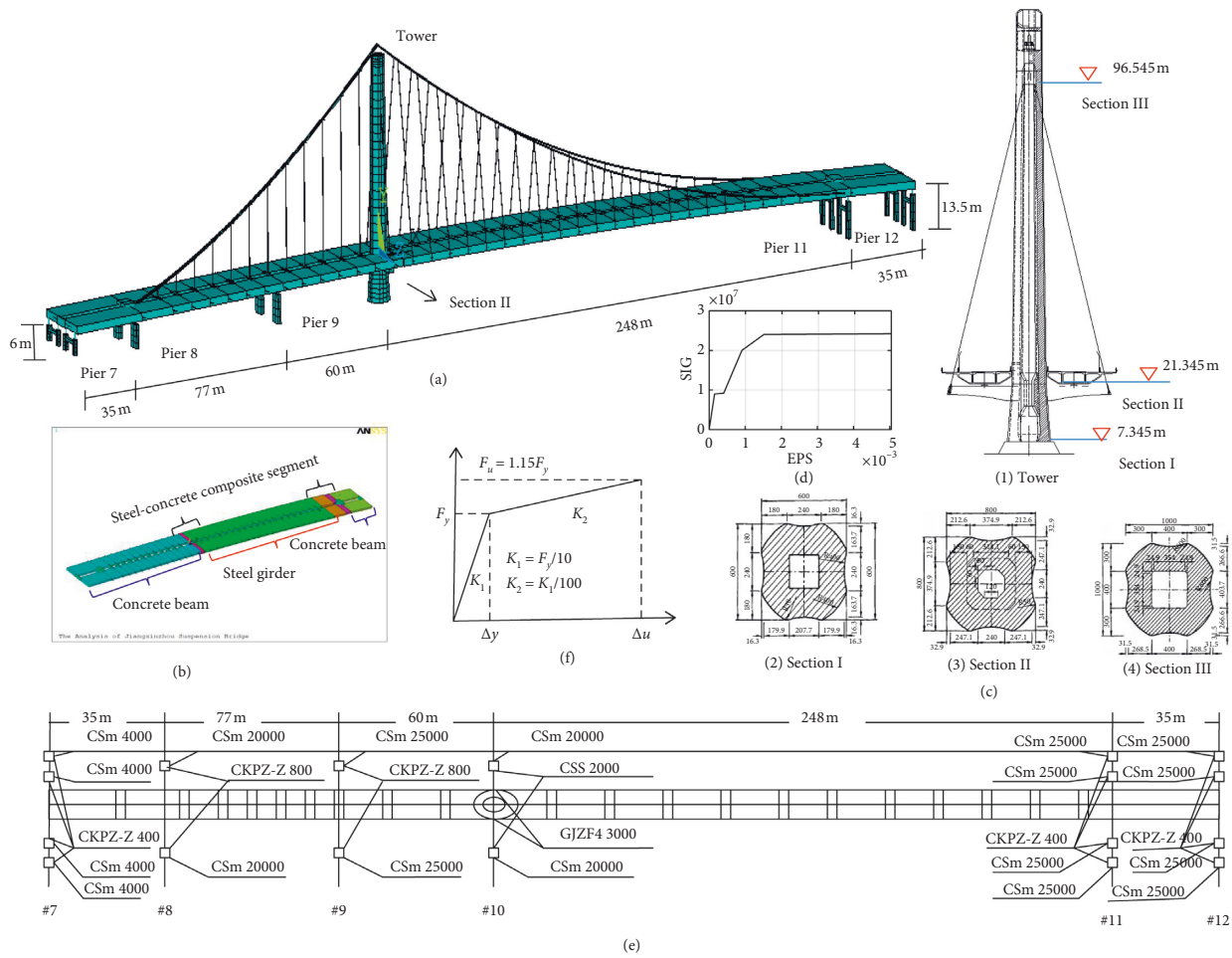

Figure 6: General configuration of the suspension bridge. (a) FE model of the bridge. (b) Modeling of the main girder. (c) Tower configuration and various sections. (d) Nonlinear model of the tower. (e) Bearing layout plan. (f) Nonlinear model of the elastic-plastic energy-dissipating bearing.

Table 1: Illustration of the bearings.

Bearing	#7	#8	#9	#10	#11	#12
Vertical	(i) Multidirectional bearing: CSm 4000 (ii) Tonnage: 4000 kN	(i) Multidirectional bearing: CSm 20000 (ii) Tonnage: 20000 kN	(i) Multidirectional bearing: CSm 25000 (ii) Tonnage: 25,000 kN	(i) Multidirectional bearing (ii) Tonnage: 20,000 kN	(i) Multidirectional bearing: CSm 2500 (ii) Tonnage: 25,000 kN	(i) Multidirectional bearing: CSm 5000 (ii) Tonnage: 5000 kN
Transversal	(i) Elastic-plastic energy-dissipating bearings: CKPZ-Z (ii) Yield load: 400 kN (iii) Maximum allowable displacement: 120 mm	(i) Elastic-plastic energy-dissipating bearings: CKPZ-Z (ii) Yield load: 800 kN (iii) Maximum allowable displacement: 120 mm	(i) Elastic-plastic energy-dissipating bearings: CKPZ-Z (ii) Yield load: 800 kN (iii) Maximum allowable displacement: 120 mm	(i) CKPZ-Q, GJZF4: 3000 kN	(i) Elastic-plastic energy-dissipating bearings: CKPZ-Z (ii) Yield load: 400 kN (iii) Maximum allowable displacement: 120 mm	(i) Elastic-plastic energy-dissipating bearings: CKPZ-Z (ii) Yield load: 400 kN (iii) Maximum allowable displacement: 120 mm
Longitudinal	—	—	—	(i) Yield load: 2000 kN (ii) Maximum allowable displacement: 100 mm	—	—

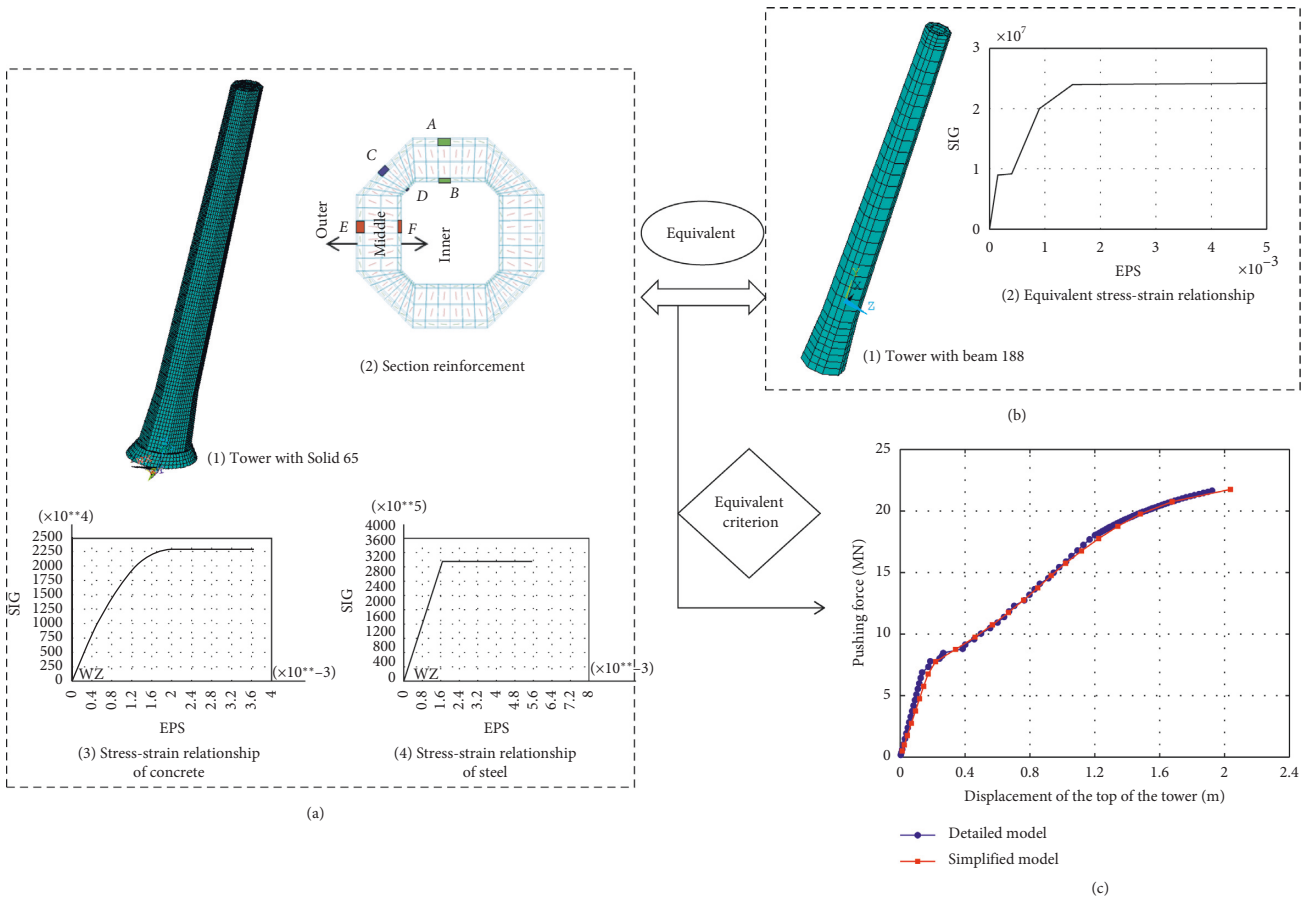

Figure 7: Main tower modeling. (a) Detailed model. (b) Simplified model. (c) Pushover analysis.

3.5. Finite Element Model Updating. Finite element model updating is described as the optimization of the difference between actual experimental data and analytical response. To determine the parameter that best reproduces the properties extracted from measurements, a global objective function combined with static property and dynamic characteristics is given as follows:

$$F_{\mathrm{ob}} = \sum_{i=1}^{N} \left| \frac{f_i' - f_i}{f_i'} \right|^2, \tag{8}$$

where f_i are subobjective functions established to measure the difference of static and dynamic characteristics, N is the number of subobjective functions, and f_i' is the final optimal value for each subobjective function, which is illustrated as

$$\begin{aligned} f_1 &= \sum_{i=1}^{3} \left| 1 - \mathrm{MAC}_i \right|^2, \\ f_2 &= \sum_{i=1}^{3} \left| \frac{F_{ci}^* - F_{ci}}{F_{ci}^*} \right|^2, \\ f_3 &= \sum_{i=1}^{3} \left| \frac{\omega_i^* - \omega_i}{\omega_i^*} \right|^2, \end{aligned} \tag{9}$$

where $\mathrm{MAC}_i = (|\phi_i^{\mathrm{T}} \phi_i^*|)/(\phi_i^{\mathrm{T}} \phi_i \phi_i^{\mathrm{T}*} \phi_i^*)$ and ϕ_i, ω_i, and F_{ci} are the modal parameters (mode and frequency) and cable force, calculated from the updated FE model, respectively. The superscript * represents the parameter identified from the monitoring data.

The subobjective functions concerned with static property are obtained by using the deformation residuals between the measurements, and analytical response from the FE model. For case 1,

$$\begin{aligned} f_4 &= \sum_{i=1}^{7} \left| \frac{d_{i1}^* - d_{i1}}{d_{i1}^*} \right|^2, \\ f_5 &= \sum_{i=1}^{7} \left| \frac{d_{ni1}^* - d_{ni1}}{d_{ni1}^*} \right|^2, \\ f_6 &= \sum_{i=1}^{7} \left| \frac{d_{si1}^* - d_{si1}}{d_{si1}^*} \right|^2, \end{aligned} \tag{10}$$

where d is the displacement of the cross sections calculated from the updated FE model. Here, the superscript * represents the measurement data, the subscript i denotes the ith section, 1 is case 1, s represents the south span, and n is the north span. Thus, f_4 is the deformation residual under symmetrical loading, and f_5 and f_6 are the deformation

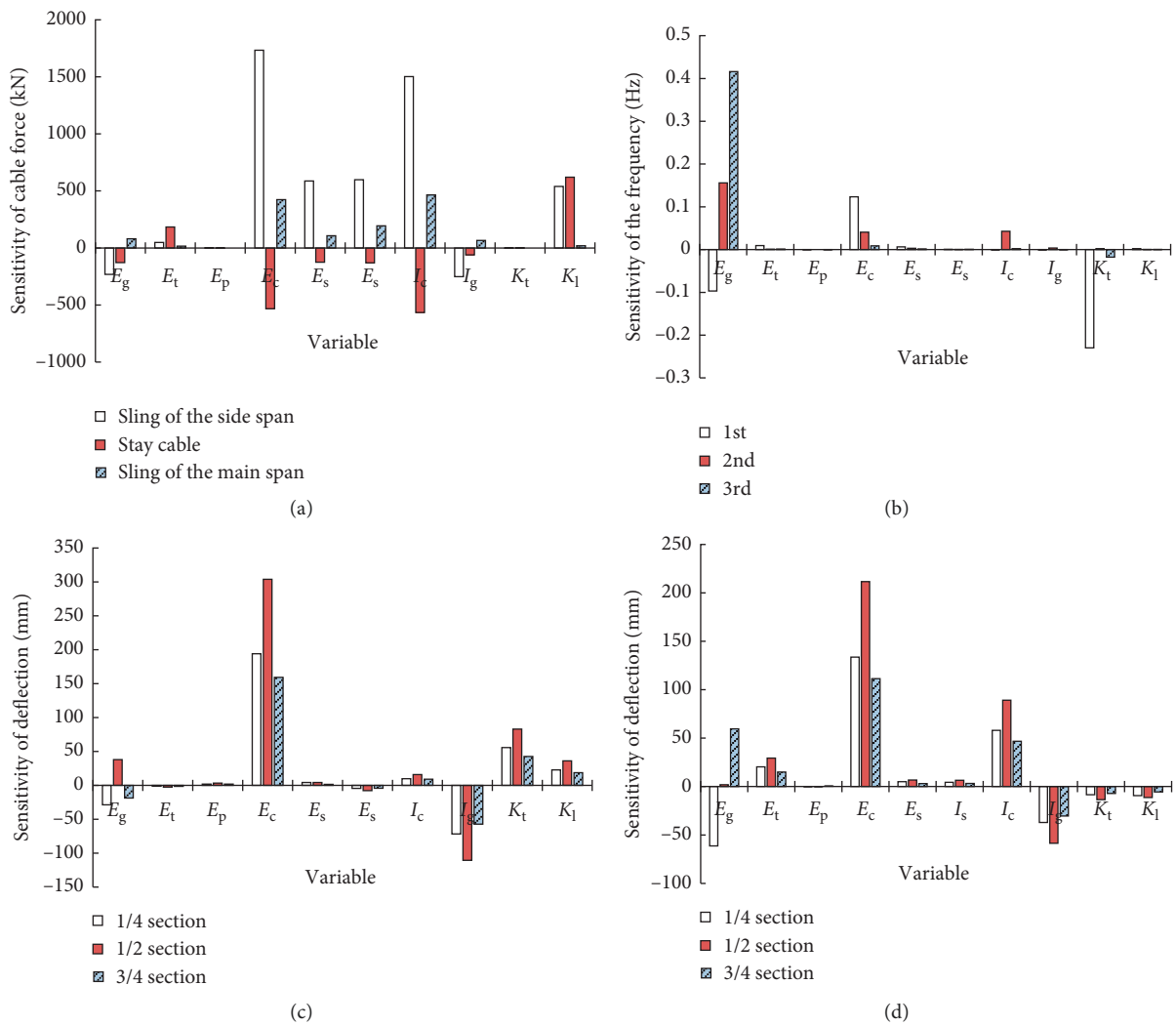

Figure 8: Sensitivity analysis. (a) Cable force. (b) Natural frequency. (c) Deflection in symmetric loading for case 1. (d) Deflection in symmetric loading for case 2.

residuals of the south span and north span, respectively, under eccentric loading. Similarly, f_7, f_8, and f_9 can be obtained for case 2. Finite element optimum design in ANSYS is applied to each subobjective function to search the theoretical optimal value f_i', and then the optimized parameter can be acquired by substituting f_i' into the global objective function (equation (8)). To avoid overfitting problems, all parameters have been limited within a $\pm 10\%$ range. The initial values are all assumed to be equal to unity, and the results are listed in Table 2.

Model analysis and static analysis are also performed on the updated model. Figures 9 and 10 show a comparison of the static deformation and modal properties extracted from measurements, with the analytical response from both the initial model and the updated model. These plots demonstrate a good match between the field measured response and the response calculated from the updated model, which possesses a higher accuracy than the initial model.

The designed value, test value, and calculated value of the cable force are illustrated in Figure 10(e). It can be observed that the measured value is consistent with the designed value. Additionally, the value calculated from the initial model is less than the measured value, but increases after updating, so the cable force identified using the updated model better matches with the experimental analysis value.

4. Seismic Fragility Analysis

Fragility curves are used to represent the seismic vulnerability of the investigated bridge. The bridge mainly consists of the towers, cables, slings, girders, and piers. The main cables and slings are flexible structures, with vibration periods in a long range, while the seismic wave rarely contains long-period components, so the fragility can be neglected. Moreover, the main girders and piers are assumed to maintain elasticity in an earthquake situation; thus, the seismic damage can be ignored for these components. Accordingly, the seismic fragility analysis of the investigated suspension bridge focuses on the tower and the elastic-plastic energy-dissipating bearing in this study.

Table 2: Variation of parameters.

Component	Main girder		Cable		Damper	
Parameter	E_g	I_g	E_c	I_c	K_t	K_l
Initial model	1	1	1	1	1	1
Updated model	1.021	1.076	1.002	1.039	0.96	0.918
Variation	2.1%	7.6%	0.2%	3.9%	−4.0%	−8.2%

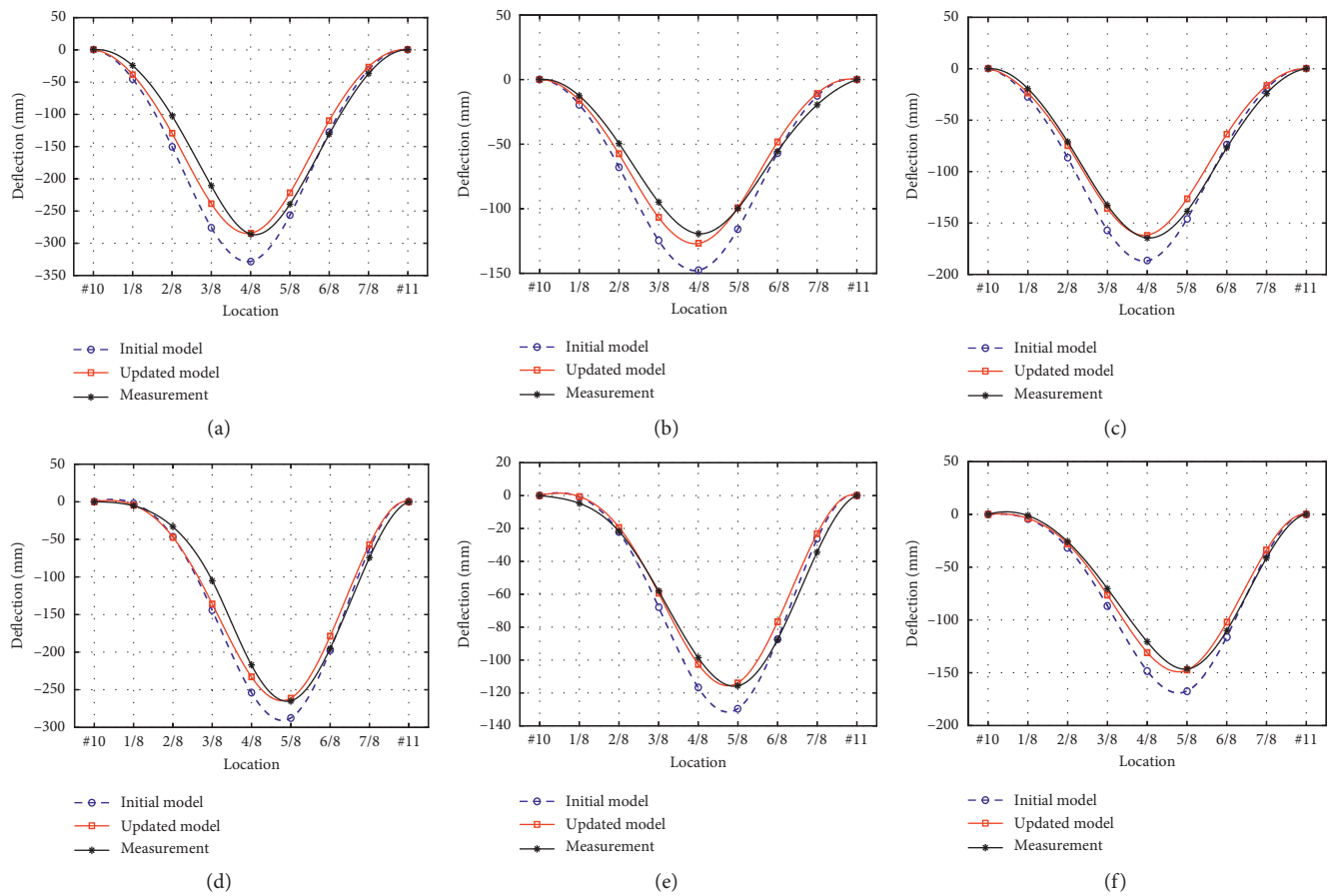

Figure 9: Comparison of the static deformation. (a) Case 1: symmetric loading. (b) Case 1: north defection with partial loading. (c) Case 1: south deflection with partial loading. (d) Case 2: symmetric loading. (e) Case 2: north defection with partial loading. (f) Case 2: south deflection with partial loading.

4.1. Ground Motion Selection. The investigated suspension bridge sits within the Nanjing potential seismic source. It is mainly affected by two seismic zones: the Tanlu seismic zone and the Yangtze River-South Yellow Sea seismic zone, which have the capacity to produce a devastating earthquake. There are 32 potential seismic sources around the engineering site contributing to the seismic hazard of the site which are identified on the Chinese seismic ground motion parameter zoning map [32] (Figure 11(a)).

According to equation (1), the seismic hazards with 10% and 2% exceedance probabilities within 50 years correspond to PGAs of 0.083 g and 0.151 g, respectively. Recognizing that the investigated bridge was designed for a hazard level of 10% in 50 years, the follow-up hazard deaggregation analysis is conducted at this level. By considering hazard contributions from certain sizes and locations, the deaggregation result is shown in Figure 11(b).

As illustrated in Figure 11(b), 90% of hazards are contributed by moderate earthquakes (4.0–6.0 M) occurring relatively close to the site (0–50 km). Given the target spectra, magnitude range, and distance range, a set of 26 ground motions are retrieved from the PEER strong motion database. Figure 12(a) illustrates the pseudoacceleration spectra of the selected ground motions (black dotted lines) and the corresponding mean spectra (black lines). It can be seen that the pseudoacceleration spectra of the selected ground motions match with the target design spectra, and the obvious dispersion highlights the inherent uncertainty between records derived from the ground motions. From the distribution of PGA (Figure 12(b)), it can be seen that the

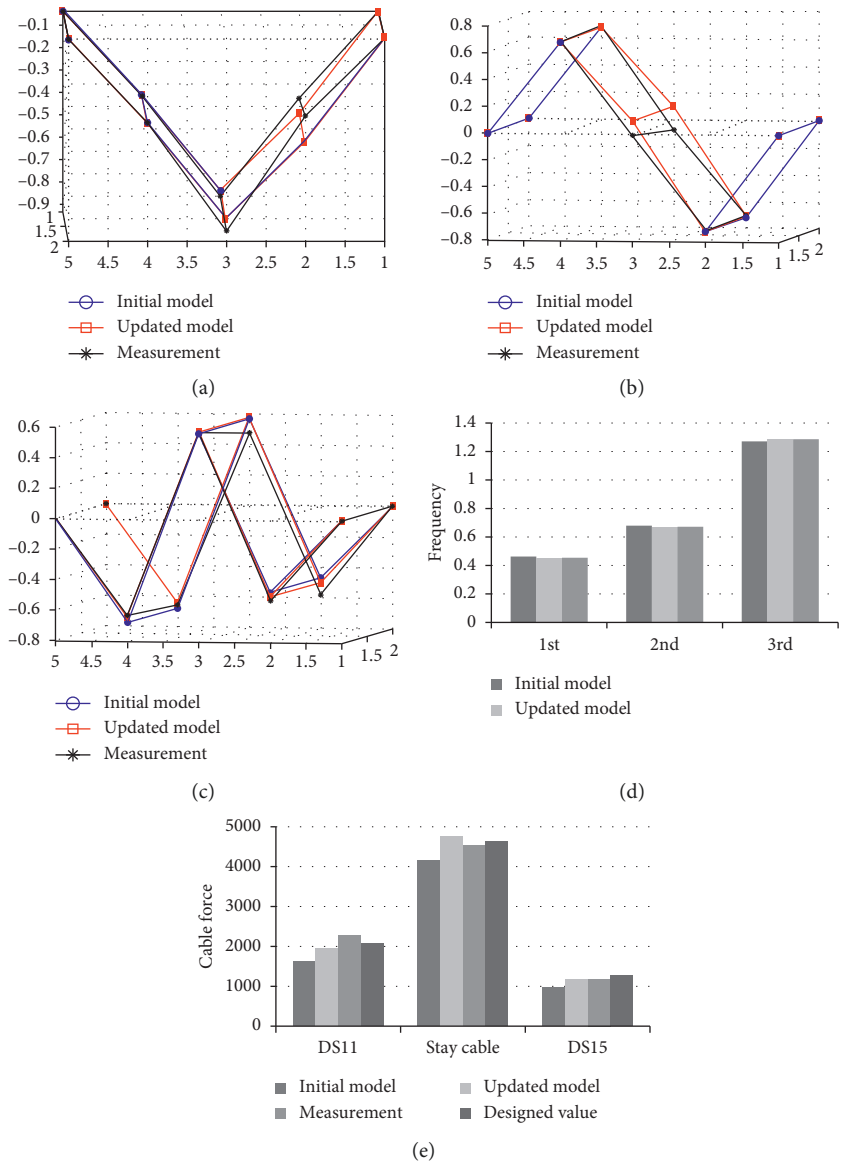

Figure 10: Comparison of dynamic test results. (a) First model. (b) Second model. (c) Third model. (d) Frequency. (e) Cable force.

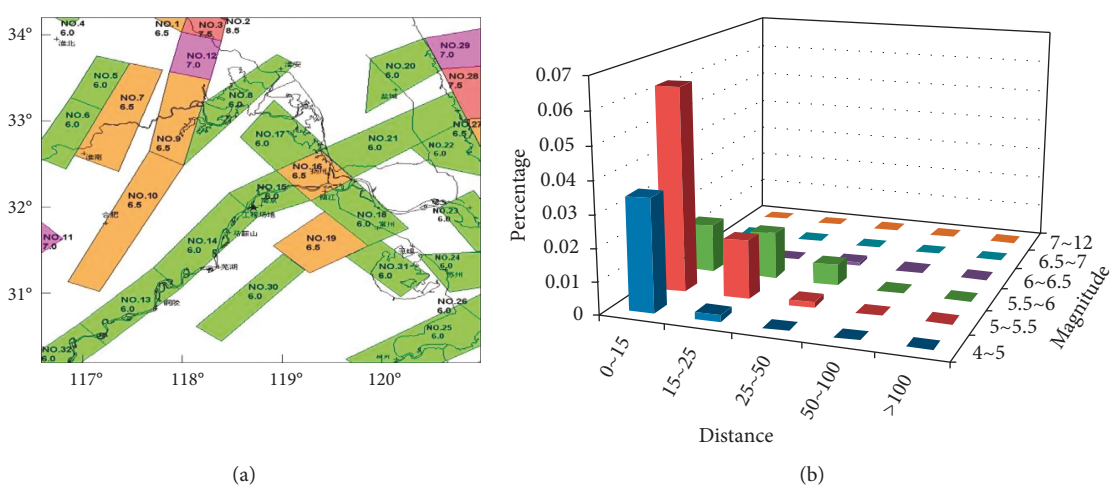

Figure 11: Probabilistic seismic hazard analysis of the site. (a) Potential seismic source. (b) Hazard deaggregation at the level of 10% in 50 years.

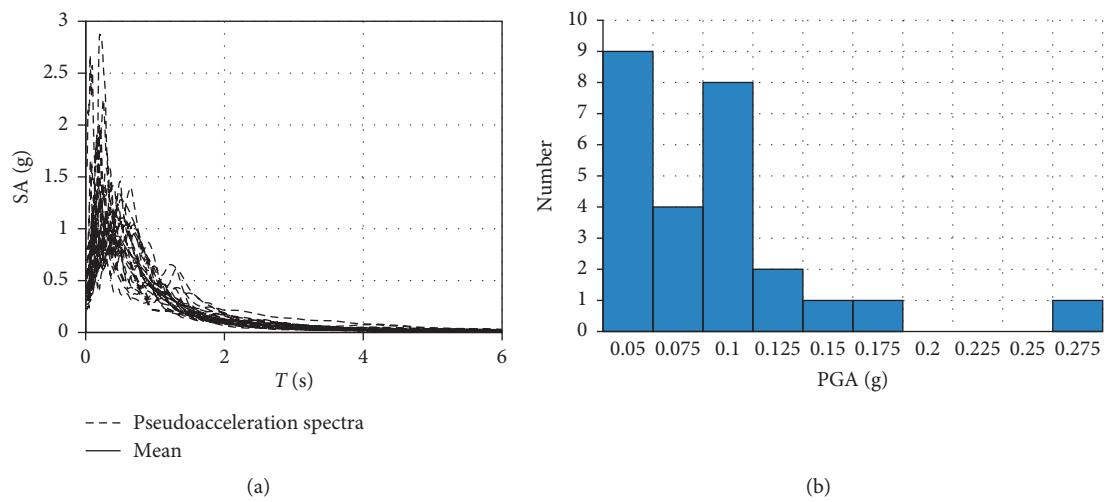

Figure 12: Property of the selected ground motions. (a) Response spectra. (b) Distribution of PGA.

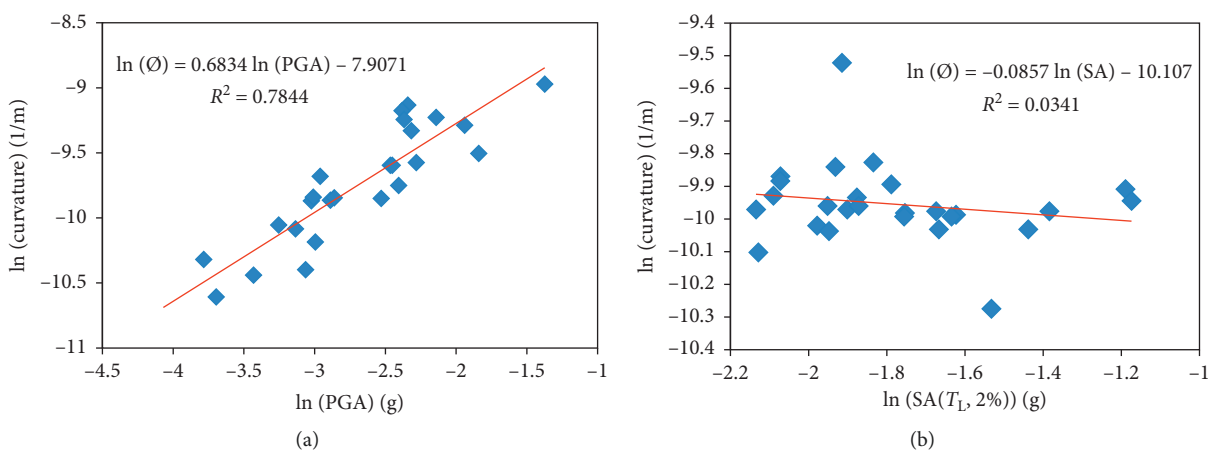

Figure 13: Probabilistic seismic demand models for the curvature of the slope section. (a) PSDM with PGA. (b) PSDM with SA.

motions cover a wide range of peak characteristics with peak ground acceleration ranging from 0.05 to 0.275 g.

Once the ground motion bin is determined, the selection of an appropriate intensity measure (IM) is the next step in fragility analysis. By means of nonlinear dynamic time-history analysis, the seismic demand of the component is estimated using the ground motions applied to the updated FE model. All of the ground motions consist of two horizontal components, which are applied to the bridge model in the longitudinal and transversal directions separately. Spectral acceleration (SA) has been widely utilized as a sufficient and practical IM in recent studies. However, taking the curvature of the slope section of the tower as an example, logistic regression between the response and PGA is compared with that of SA, and the results plotted in Figure 13 show that using PGA as an IM fits better than SA. Therefore, PGA is adopted as the IM for fragility analysis in this study. The developed PSDMs of the tower section, as well as the median estimates and dispersion estimates, are shown in Figure 13(a).

4.2. Damage Index and Limit States. In fragility analysis, the structural capacity is described in terms of damage index (DI). Different DIs for various components require specific limit state (LS) values, which are commonly obtained from engineering judgments or experiments [33]. Four LSs defined by Hazus [34] have been widely used in structural performance-based earthquake engineering. They are slight (SL), moderate (MO), extensive (EX), and complete (CO) damage. In this study, the definition of the DI for the bearing mainly refers to regular bridges, and the relative bearing displacement between the pier and the girder has been adopted [35]. The allowable bearing displacement is defined as the limit value of EX damage, and half of this distance is MO damage. Once the relative bearing displacement surpasses half of the masonry plate, that is, the girder slides off the masonry plate, the bearing is deemed CO damaged. Four LSs of the bearing are listed in Table 3.

As little knowledge about the DI for the tower of a suspension bridge is available in the literature, a pushover analysis is conducted on the detailed tower model to define

Table 3: Quantified limit states of various components.

Component	DI	Slight	Moderate	Extensive	Complete
Section of the tower	Curvature ϕ	$1.94E-4 \le \phi < 5.72E-4$	$5.72E-4 \le \phi < 1.33E-3$	$1.33E-3 \le \phi < 3.94E-3$	$\phi \ge 3.94E-3$
Tower displacement	Drift ratio	$0.0016 \le u < 0.0036$	$0.0036 \le u < 0.01$	$0.01 \le u < 0.018$	$u \ge 0.018$
Bearing (#7, 12)	Disp. (mm)	$40 \le \Delta < 60$	$60 \le \Delta < 120$	$120 \le \Delta < 400$	$\Delta \ge 400$
Bearing (#8, 9, 11)	Disp. (mm)	$40 \le \Delta < 60$	$60 \le \Delta < 120$	$120 \le \Delta < 800$	$\Delta \ge 800$
Bearing (#10)	Disp. (mm)	$33.3 \le \Delta < 50$	$50 \le \Delta < 100$	$100 \le \Delta < 800$	$\Delta \ge 800$

Note. Disp. = displacement.

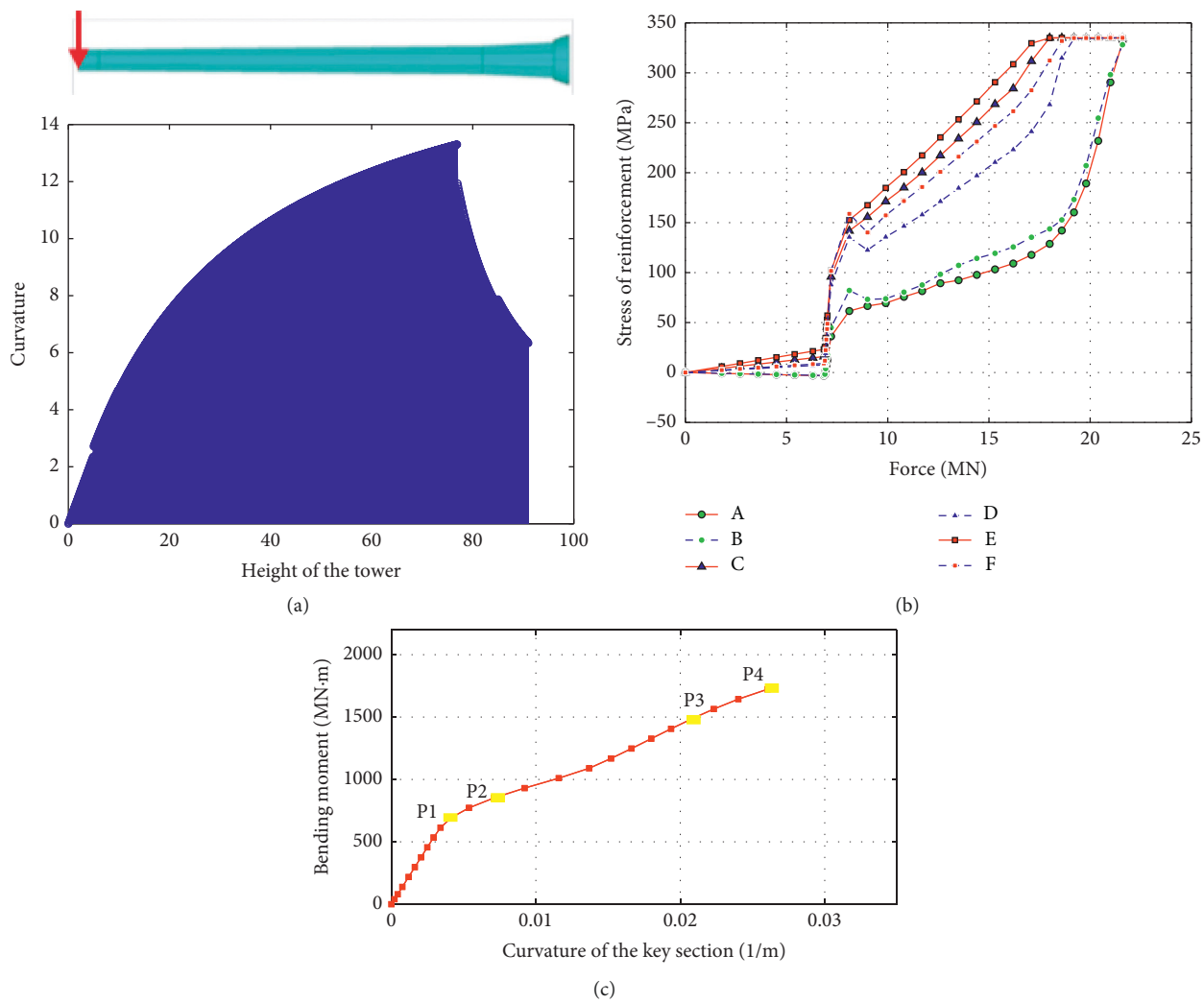

Figure 14: Determination of the LS for the key section. (a) Curvature of the main tower. (b) Steel stress in the key section. (c) $M-\phi$ curves of the key section.

the failure mode and locate the most vulnerable part of the tower. In elastic range, the maximum sectional curvature occurs on the slope section shown in Figure 14(a). Additionally, during the pushover analysis, the first crack appears in the slope section and subsequently steps into the plastic stage. When reinforcement stress increases sharply, the section eventually breaks. Thus, the slope section is chosen as a key section to study the seismic fragility of the tower. Based on the configuration of the sectional reinforcement in Figure 7(a), variation of the reinforcement stress is illustrated in Figure 14(b). The following stages are visible: (1) In the elastic stage, the stress of reinforcement grows linearly with the increase of push force. (2) Some minor cracks appear on the slope section initially, and the reinforcement stress increases sharply from outer to inner layers. (3) As the cracks grow, the outer reinforcement gradually increases and then yields. (4) Finally, extensive damage to the inner reinforcement occurs, and the tower breaks. Corresponding to the phenomenon described above, four characteristic points (P1, P2, P3, and P4) are picked on

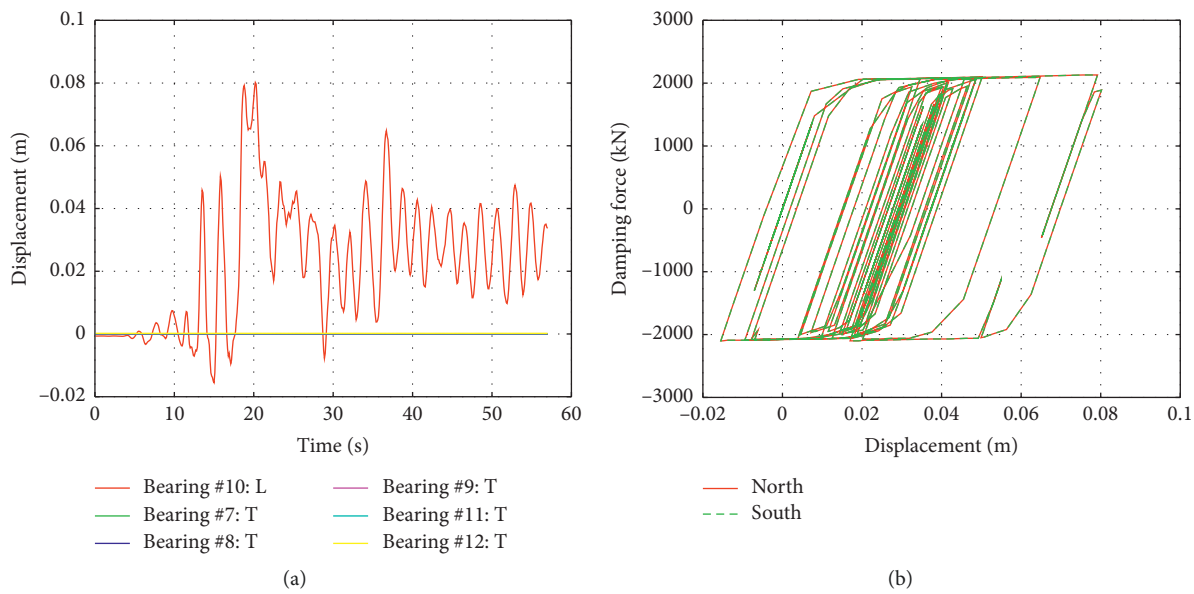

Figure 15: Longitudinal earthquake response of the bearing. (a) Bearings #7~12 (L: longitudinal; T: transverse). (b) Force-displacement hysteretic curves of the damper.

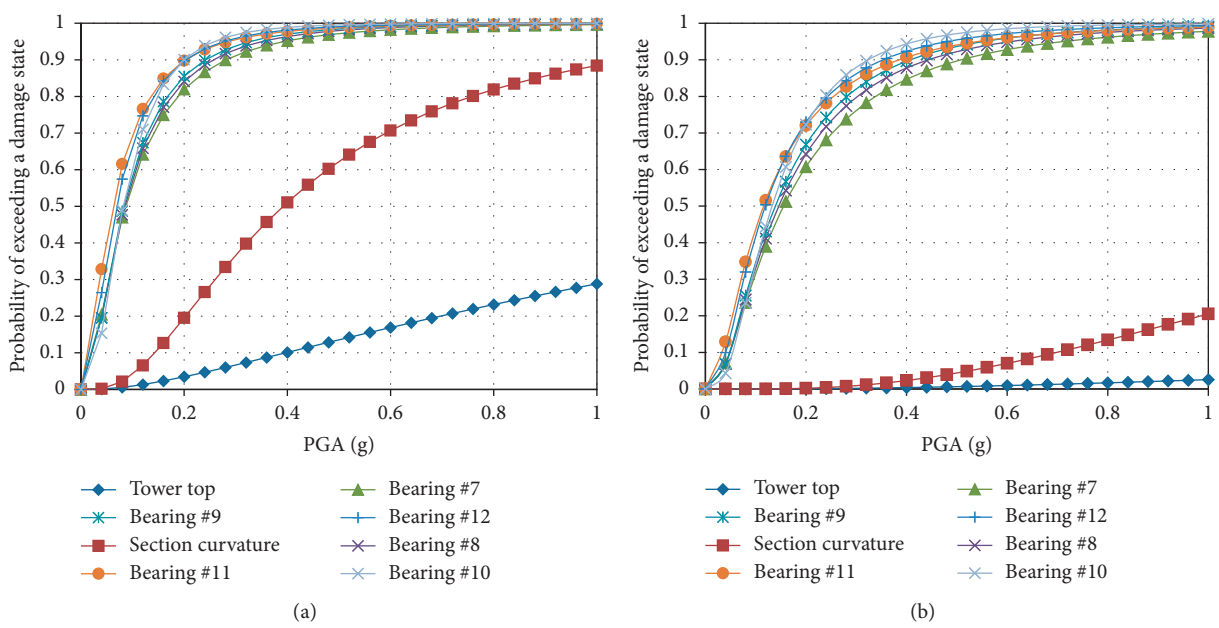

Figure 16: Continued.

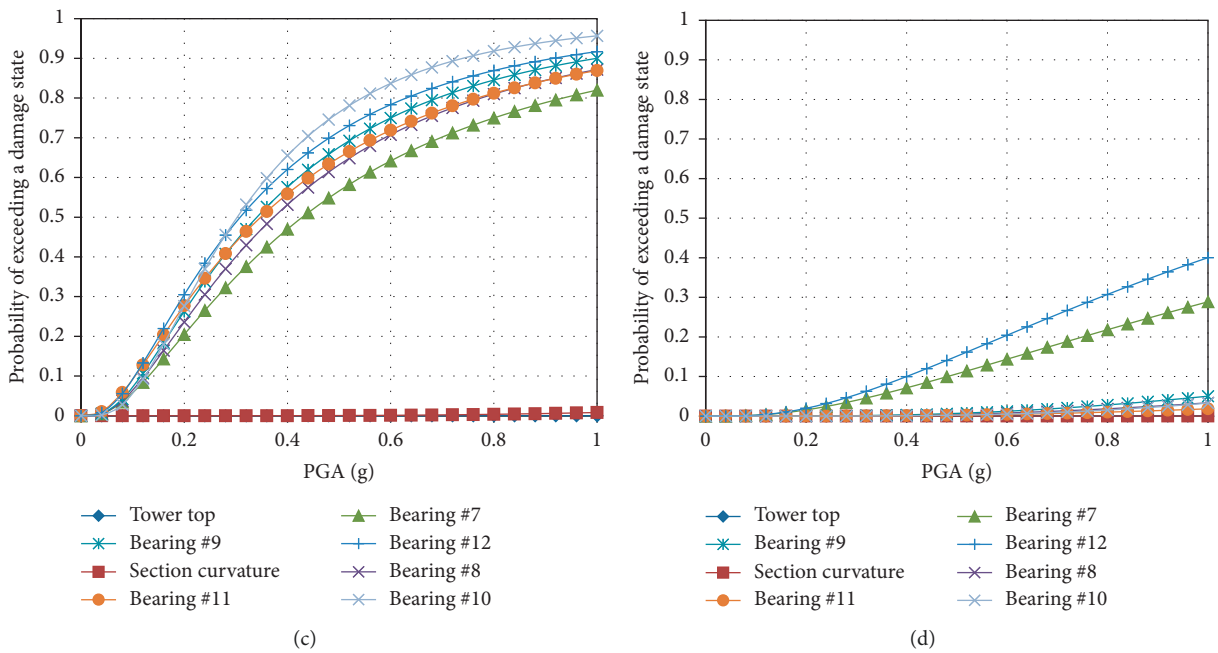

Figure 16: Longitudinal fragility curves of components. (a) Slight damage. (b) Moderate damage. (c) Extensive damage. (d) Complete damage.

the $M-\phi$ curves of the key section shown in Figure 14(c). In addition, displacement of the top of the tower is selected as another fragile component to describe the damage to the tower, the limit states of which can be obtained from the correlation curve between push force and top displacement.

The seismic behavior of these major components governs the damage and failure modes of the suspension bridge. In conclusion, the DI for various components is defined in terms of bearing displacement, displacement of the top of the tower, and curvatures of the key section of the tower. Table 3 summarizes the definitions of DI criteria and corresponding LS values.

4.3. Seismic Fragility Analysis Result. To explore the seismic performance of the suspension bridge accurately, fragility analysis is conducted from the longitudinal and transversal directions separately. In longitudinal seismic excitation, the lateral displacement of the bearing plotted in Figure 15(a) is zero, indicating that no transverse vibration occurs, and the vibration in the longitudinal direction is decoupled with lateral vibration. Accordingly, the lateral reaction can be neglected in longitudinal seismic analysis. In addition, it can be seen from Figure 15(b) that the force-deformation skeleton curves of the #10 south bearing are consistent with those of the north bearing, so only one side needs to be accounted for in this study.

Combined with the component damage index and PSDMs, the fragility curves for different damage states are calculated according to equation (4). As seen in Figure 16, the bearing is more vulnerable than the tower in longitudinal seismic analysis. For all bearings, the damage probability of the #10 bearing is largest when the first three damage states occur because the maximum allowable displacement of the #10 bearing is smaller than that of others. When complete damage occurs, namely, the main girder slides from the edge of the masonry plate, #7 and #12 bearings are prone to collapse as their masonry plate width is 800 mm, while #8, #9, #10, and #11 bearings are 1600 mm wide.

In transversal analysis, only the lateral response of the bearings is considered. It should be noted that the lateral displacement of the #10 bearing is zero, as two isolating bearings were set between the tower and the girder to limit transversal displacement. Consequently, transversal fragility focuses on the tower and #7, #8, #9, #11, and #12 bearings, and the results are provided in Figure 17. It can be observed that the #12 bearing has the highest fragility probability in all four limit states, while the #9 bearing has the lowest. Additionally, the fragility probability from high to low is consistent in four states, that is, #12 > #7 > #11 > #8 > #9. This is because the masonry plate width of the #12 and #7 bearings is smaller than that of others. Overall, the bearings remain the most vulnerable component. It is also found that the effect of the damper is minimal for slight to moderate earthquakes and high for strong earthquakes in the case of complete damage. For slight and moderate damage states, the dampers do not show any visible impact on the fragility curves of the bridges. In complete damage states, the probability of fragility decreases obviously, which could be attributed to the energy consumption of the dampers.

4.4. Result Comparison between Initial and Updated Models. To evaluate the impact that variation of the updating parameter has on the seismic vulnerability of the bridge, a comparison of fragility curves between the initial and

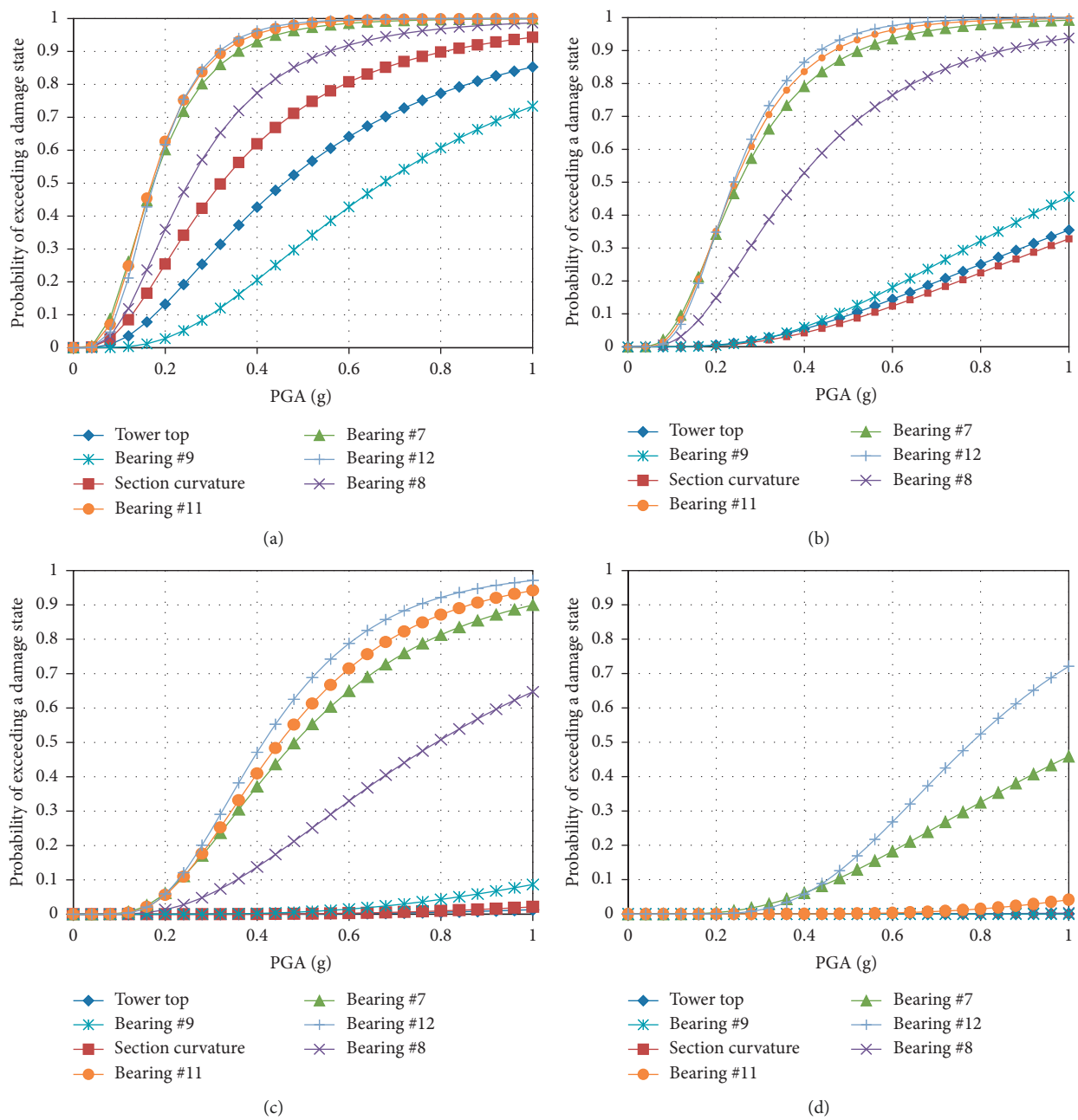

Figure 17: Transversal fragility curves of components. (a) Slight damage. (b) Moderate damage. (c) Extensive damage. (d) Complete damage.

updated models is conducted. In the longitudinal direction, it can be seen from the above analysis that the fragility curves of bearings are almost the same, so it only focuses on the comparison of the #10 bearing here. In the transversal direction, the most vulnerable parts are #12, #7, and #11 bearings, so only comparison of these bearings is considered here. The results are plotted as follows.

Comparison results provided in Figure 18 illustrate that the fragility curves change from the initial to the updated model, and the probability of exceeding a given damage state generally increases with different degrees as expected. The fragility curves for extensive damage change notably, especially for the #10 bearing in the longitudinal direction. This is attributed to the yield stiffness of the #10 bearing in the longitudinal direction, which is reduced by 8.2% in the modification. The vulnerability of #7 and #12 bearings in the lateral direction also increases because of a 4% stiffness reduction of the bearing.

5. Conclusions

A typical self-anchored suspension bridge was used as an example to illustrate the practical application of structural health monitoring data for the evaluation of structural fragility in this study. Using design information and service

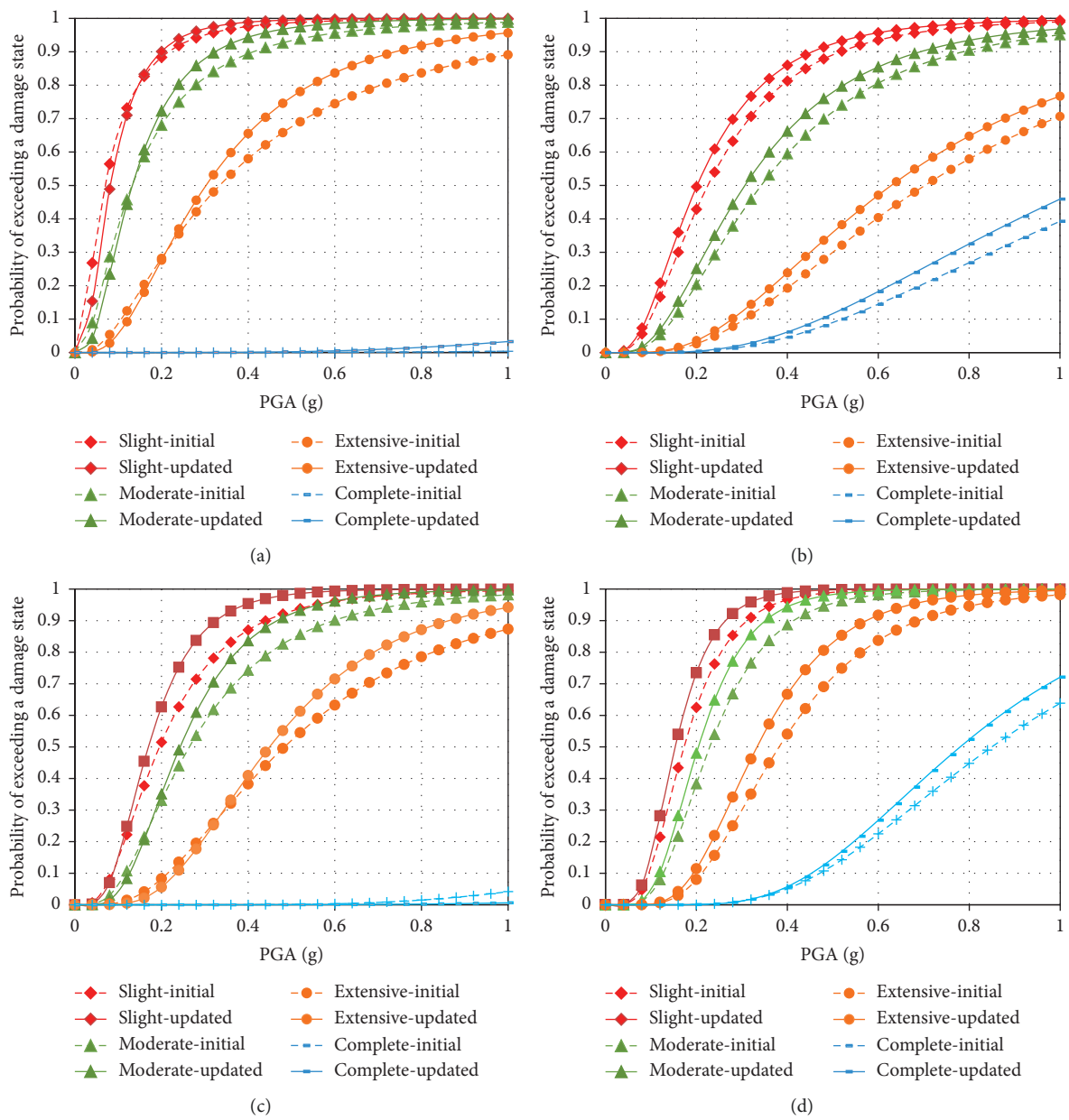

Figure 18: Fragility comparison between the initial model and the updated model. (a) Longitudinal fragility curves of bearing #10. (b) Transversal fragility curves of bearing #7. (c) Transversal fragility curves of bearing #11. (d) Transversal fragility curves of bearing #12.

life experimental data, FE model updating was undertaken according to the optimization of an objective function. This is described in terms of the difference between the measured bridge response and the FE model response. Prior to optimization, a sensitivity analysis was conducted to determine the updating parameters that cause a larger change in structural properties when varying their assigned value. Based on the updated model, the fragility curves are researched. The ground motions used in the seismic demand analysis were selected according to the PSHA deaggregation result and can help to determine the most likely earthquake at the site according to the PEER database. In this manner, the ground motions are more realistic and the seismic demand models are closer to the actual ones.

Conclusions about the seismic performance of the self-anchored suspension bridge are obtained as follows: The longitudinal response of the bridge is mainly related to the constraints between the tower and the girder. For the floating-type bridge, large displacement will be produced that is harmful to bearings. In the transverse direction, fixed constraints between piers and girders will induce a large seismic response because of the nonuniform distribution of girder mass, which is bad for the transverse shearing resistance of the bearing. Consequently, the bearing is the most vulnerable part of the self-anchored suspension bridge. The adoption of elastic-plastic energy-dissipating bearings can decrease the seismic reaction of the bearing and improve its seismic performance. From the fragility results, it can be

seen that the effect of the damper is minimal for slight to moderate earthquakes and high for strong earthquakes in the case of complete damage. For slight and moderate damage states, the dampers do not display any visible impact on the fragility curves of the bridges. Compared with the bearing, no serious damage or complete destruction of the tower will occur under a predictable earthquake.

Data Availability

The response data of the FE model used to support the findings of this study are available from the corresponding author upon request.

Conflicts of Interest

The authors declare that there are no conflicts of interest regarding the publication of this paper.

Acknowledgments

This research was financially supported by the National Key R&D Program of China (no. 2018YFC0705601), Jiangsu Distinguished Young Scholars Fund (no. BK20160002), and National Science Foundation of China (grant nos. 51578139 and 51608110).

References

[1] S. Banerjee and M. Shinozuka, "Nonlinear static procedure for seismic vulnerability assessment of bridges," *Computer-Aided Civil and Infrastructure Engineering*, vol. 22, no. 4, pp. 293–305, 2007.

[2] M. Choine, A. Connor, and J. Padgett, "Comparison between the seismic performance of integral and jointed concrete bridges," *Journal of Earthquake Engineering*, vol. 19, no. 1, pp. 172–191, 2015.

[3] J. B. Mander, R. P. Dhakal, N. Mashiko, and K. M. Solberg, "Incremental dynamic analysis applied to seismic financial risk assessment of bridges," *Engineering Structures*, vol. 29, no. 10, pp. 2662–2672, 2007.

[4] A. Ozgur, Y. Ahmet, and C. Alp, "Analytical fragility curves for ordinary highway bridges in Turkey," *Earthquake Spectra*, vol. 27, no. 4, pp. 971–996, 2011.

[5] D. H. Tavares, J. E. Padgett, and P. Paultre, "Fragility curves of typical as-built highway bridges in Eastern Canada," *Engineering Structures*, vol. 40, pp. 107–118, 2012.

[6] U. Yazgan, "Empirical seismic fragility assessment with explicit modeling of spatial ground motion variability," *Engineering Structures*, vol. 100, pp. 479–489, 2015.

[7] H. Hwang, J. B. Liu, and Y. H. Chiu, "Seismic fragility analysis of highway bridges," Tech. Rep. MAEC RR-4 Project, Mid-America Earthquake Center, Urbana, IL, USA, 2001.

[8] S. Argyroudis and A. M. Kaynia, "Fragility functions of highway and railway infrastructure," in *SYNER-G: Typology Definition and Fragility Functions for Physical Elements at Seismic Risk. GGEE 27*, K. Pitilakis, H. Crowley, and A. M. Kaynia, Eds., Springer, Berlin, Germany, 2014.

[9] S. Argyroudis, S. Mitoulis, A. M. Kaynia, and M. G. Winter, *Fragility Assessment of Transportation Infrastructure Systems Subjected to Earthquakes*, Geotechnical Special Publication (GSP 292), Auburn, IN, USA, 2018.

[10] G. Tsionis and M. N. Fardis, "Fragility functions of road and railway bridges", in *SYNER-: Typology Definition and Fragility Functions for Physical Elements at Seismic Risk*, vol. 27 of Geotechnical, Geological and Earthquake Engineering, K. Pitilakis, H. Crowley, and A. M. Kaynia, Eds., Springer, Dordrecht, Netherlands, 2014.

[11] Y. Pan, A. K. Agrawal, M. Ghosn, and S. Alampalli, "Seismic fragility of multispan simply supported steel highway bridges in New York State. II: fragility analysis, fragility curves, and fragility surfaces," *Journal of Bridge Engineering*, vol. 15, no. 5, pp. 462–472, 2010.

[12] N. Parool and D. C. Rai, "Seismic fragility of multispan simply supported bridge with drop spans and steel bearings," *Journal of Bridge Engineering*, vol. 20, no. 12, Article ID 04015021, 2015.

[13] A. Mosleh, M. S. Razzaghi, J. Jara, and H. Varum, "Seismic fragility analysis of typical pre-1990 bridges due to near- and far-field ground motions," *International Journal of Advanced Structural Engineering*, vol. 8, no. 1, pp. 1–9, 2016.

[14] C. Li, H.-N. Li, H. Hao, K. Bi, and B. Chen, "Seismic fragility analyses of sea-crossing cable-stayed bridges subjected to multi-support ground motions on offshore sites," *Engineering Structures*, vol. 165, pp. 441–456, 2018.

[15] Y. T. Pang, X. Wu, G. Y. Shen, and W. C. Yuan, "Seismic fragility analysis of cable-stayed brides considering different sources of uncertainties," *Journal of Bridge Engineering*, vol. 19, no. 4, Article ID 04013015, 2014.

[16] M. N. Choine, A. O'Connor, and J. E. Padgett, "A seismic reliability assessment of reinforced concrete integral bridges subject to corrosion," *Key Engineering Materials*, vol. 569-570, pp. 366–373, 2013.

[17] J. Ghosh and P. Sood, "Consideration of time-evolving capacity distributions and improved degradation models for seismic fragility assessment of aging highway bridges," *Reliability Engineering & System Safety*, vol. 154, pp. 197–218, 2016.

[18] M. Torbol, H. Gomez, and M. Feng, "Fragility analysis of highway bridges based on long-term monitoring data," *Computer-Aided Civil and Infrastructure Engineering*, vol. 28, no. 3, pp. 178–192, 2013.

[19] S. Karapetrou, M. Manakou, D. Bindi, B. Petrovic, and K. Pitilakis, ""Time-building specific" seismic vulnerability assessment of a hospital RC building using field monitoring data," *Engineering Structures*, vol. 112, pp. 114–132, 2016.

[20] L. Sgambi, E. Garavaglia, N. Basso, and F. Bontempi, "Monte Carlo simulation for seismic analysis of a long span suspension bridge," *Engineering Structures*, vol. 78, pp. 100–111, 2014.

[21] D. Karmakar, S. Ray-Chaudhuri, and M. Shinozuka, "Finite element model development, validation and probabilistic seismic performance evaluation of Vincent Thomas suspension bridge," *Structure and Infrastructure Engineering*, vol. 11, no. 2, pp. 223–237, 2015.

[22] E. Choi, R. DesRoches, and B. Nielson, "Seismic fragility of typical bridges in moderate seismic zones," *Engineering Structures*, vol. 26, no. 2, pp. 187–199, 2004.

[23] R. Karthik, D. Reginald, and E. P. Jamie, "Analytical fragility curves for multispan continuous steel girder bridges in moderate seismic zones," *Transportation Research Record: Journal of the Transportation Research Board*, vol. 2202, no. 1, pp. 173–182, 2010.

[24] B. G. Nielson and R. DesRoches, "Analytical seismic fragility curves for typical bridges in the central and Southeastern

United States," *Earthquake Spectra*, vol. 23, no. 3, pp. 615–633, 2007.

[25] W. P. Wu, L. F. Li, and X. D. Shao, "Seismic assessment of medium-span concrete cable-stayed bridges using the component and system fragility functions," *Journal of Bridge Engineering*, vol. 21, no. 6, Article ID 04016027, 2016.

[26] J.-P. Wang, D. Huang, C.-T. Cheng, K.-S. Shao, Y.-C. Wu, and C.-W. Chang, "Seismic hazard analyses for Taipei city including deaggregation, design spectra, and time history with excel applications," *Computers & Geosciences*, vol. 52, pp. 146–154, 2013.

[27] C. A. Cornell, "Engineering seismic risk analysis," *Bulletin of the Seismological Society of America*, vol. 58, no. 5, pp. 1583–1606, 1968.

[28] R. K. McGuire and W. J. Arabasz, "An introduction to probabilistic seismic hazard analysis," in *Geotechnical and Environmental Geophysics*, vol. 1, pp. 333–354, Society of Exploration Geophysicists, Tulsa, OK, USA, 1990.

[29] US Nuclear Regulatory Commission, *Regulatory Guide 1.208: A Performance-Based Approach to Define the Site-Specific Earthquake Ground Motions*, US Nuclear Regulatory Commission, Washington D.C, USA, 2007.

[30] J. Zhang and Y. Huo, "Evaluating effectiveness and optimum design of isolation devices for highway bridges using the fragility function method," *Engineering Structures*, vol. 31, no. 8, pp. 1648–1660, 2009.

[31] C. A. Cornell, F. Jalayer, R. Hamburger, and D. Foutch, "Probabilistic basis for 2000 SAC Federal Emergency Management Agency steel moment frame guidelines," *Journal of Structural Engineering*, vol. 128, no. 4, pp. 526–533, 2002.

[32] GB18306-2001, *GB18306-2001: Seismic Ground Motion Parameter Zonation Map of China*, China Standard Press, Beijing, Chaina, 2001.

[33] F. Casciati, G. P. Cimellaro, and M. Domaneschi, "Seismic reliability of a cable-stayed bridge retrofitted with hysteretic devices," *Computers & Structures*, vol. 86, no. 17-18, pp. 1769–1781, 2008.

[34] FEMA, *HAZUS99 User's Manual*, Federal Emergency Management Agency, Washington, DC, USA, 1999.

[35] J. E. Padgett and R. DesRoches, "Methodology for the development of analytical fragility curves for retrofitted bridges," *Earthquake Engineering & Structural Dynamics*, vol. 37, no. 8, pp. 1157–1174, 2008.